

Interaction of Mass Transport and Reaction Kinetics during Electrocatalytic CO Oxidation in a Thin-Layer Flow Cell

D. Zhang,[†] O. Deutschmann,[†] Y. E. Seidel,[‡] and R. J. Behm^{*,‡}

Institute for Chemical Technology and Polymer Chemistry, Karlsruhe Institute of Technology, D-76131 Karlsruhe, Germany, and Institute of Surface Chemistry and Catalysis, Ulm University, D-89069 Ulm, Germany

Received: July 26, 2010; Revised Manuscript Received: November 19, 2010

The interplay between electrocatalytic CO oxidation kinetics and mass transport in a thin-layer flow cell with a polycrystalline platinum electrode was experimentally studied and numerically simulated. The experiments were performed in a flow cell under controlled electrolyte flow. The computations are based on four different models for mass transport, coupled with a three-step reaction mechanism for CO oxidation that includes surface coverage effects. A zero-dimensional model neglecting mass transport effects on the overall reaction rate is applied to verify the effect of the kinetic parameters on the Faradaic current qualitatively. Transport models of increasing complexity, one-, two-, and three-dimensional, are used to analyze the impact of diffusion and convection on the total reaction rate in the flow cell. The numerical simulation, based on a time-resolved three-dimensional transport model coupled with the electrocatalytic kinetics, resolves profiles of temporal and spatial concentrations, velocities, and surface coverages. Mass transfer limitations of the electrocatalytic reaction rate are primarily caused by CO diffusion normal to the electrode. Both the two- and the three-dimensional models can quantitatively predict the Faradaic current as a function of potential measured in the experimental setup.

1. Introduction

Similar to catalytic reactions, mass transport of reactants and products plays an important role in electrocatalytic reactions.^{1,2} The importance of mass transport on the resulting overall reaction rate, which in general may be limited either by the actual local catalytic reaction rate (“kinetic limitation”) or by mass transport effects (“transport limitation”), has been well recognized. Mass transport may affect also the reaction pathways and in particular the product distribution during a catalytic or electrocatalytic reaction,^{3–7} which for electrocatalytic reactions was discussed in detail recently.⁶ For a detailed understanding of the overall conversion in an electrochemical cell, the coupling of mass transport and surface reaction processes has to be described. In the present contribution, we report on a combined experimental and simulation study on the coupling between convective and diffusive mass transport and chemical reaction during CO electro-oxidation in a cylindrical thin-layer flow cell, under controlled external conditions. Although the transport characteristics in such kind of flow cell are significantly more complicated than, for example, the homogeneous flow pattern in a rotating disk electrode setup,^{8,9} it was used because it affords the possibility of simultaneous detection of the Faradaic current and of volatile reaction products via mass spectrometric detection (differential electrochemical mass spectrometry – DEMS), which shall be employed in future studies of more complex reactions such as methanol oxidation.

The electro-oxidation of CO on platinum electrodes is one of the fundamental electrocatalytic reactions that has been studied extensively.^{10–21} Depending on the experimental conditions, the reaction rate may be strongly affected by mass

transport due to the low concentration of dissolved CO in the electrolyte. Mass transport may play a significant role during continuous oxidation of CO (“CO bulk oxidation”),²² while for the electro-oxidation of preadsorbed CO (“CO_{ad} stripping”) mass transport effects are absent. Although this is well-known, the influence of (externally) enforced mass transport on the reaction characteristics has, to the best of our knowledge, not been studied quantitatively so far, including model studies considering diffusive transport in the description of the reaction rate.^{23,24}

The quantitative interpretation of the experimentally determined Faradaic current demands the understanding of the coupling between mass transport of electrolyte (convection) and in the electrolyte (diffusion), on the one hand, and the kinetics of the electrocatalytic reaction on the electrode surface, on the other hand, where the latter is governed by the temporally and spatially varying fluid concentrations and surface coverages. Fuhrmann et al. recently studied the effect of electrolyte flow on the mass transport limited H₂ oxidation current by applying a macroscopic model and a generalization of a Leveque-type asymptotic estimate for circular electrodes.^{25–27} These authors also described the adsorption of CO by the same model described above.²⁸ Other studies focused on the reaction kinetics, but did not include effects of electrolyte transport.^{24,29–32} Bonnefont et al.³³ addressed the stability of a laterally uniform CO adlayer on a Pt electrode surface during CO bulk oxidation by stationary potential probing and analyzed the resulting spatial pattern formation based on an extended version of the kinetic model for CO electro-oxidation by Koper et al.²⁹

Because the measured electrocatalytic reaction rate is often limited by concentration gradients, caused by relatively slow diffusion in the liquid phase, the local concentration of the reactant species and their distribution vertical to the electrode are decisive parameters for the overall reaction rate. In other words, the catalytically active sites experience temporarily and

* Corresponding author. E-mail: juergen.behm@uni-ulm.de.

[†] Karlsruhe Institute of Technology.

[‡] Ulm University.

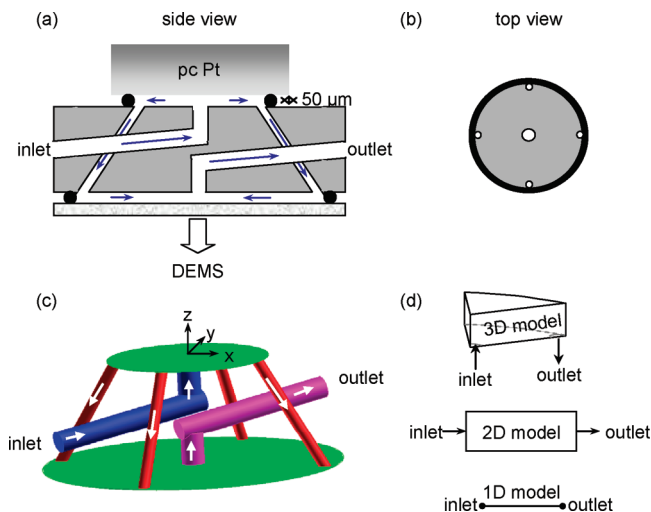


Figure 1. Schematic description of the dual thin-layer flow cell (a,b) and illustration of the electrolyte flow in the cell (c). (d) Overview of various geometric models for the description of mass transport during the reaction (1D, 2D, and 3D models).

spatially varying reaction conditions. In the present study, the mean field approximation²⁴ is applied to consider both surface reaction kinetics and spatially resolved mass transport effects in numerical simulations.^{34–36} Several transport models of varying complexity and simple reaction kinetics for CO oxidation, including spatially resolved coverages and reaction rates, are used to understand the level of model accuracy needed to adequately describe the mass transport behavior in the cylindrical flow cell used in these experiments and to interpret the measurements. The kinetic model used includes CO adsorption, desorption, and oxidation, and the influence of the initial surface coverage of adsorbed CO. Finally, two experimental procedures are numerically simulated, the oxidation of a preadsorbed CO monolayer (“CO_{ad} stripping”), and the oxidation of CO in a continuous flow of electrolyte (“CO bulk oxidation”), where the former reaction is used to derive kinetic reaction parameters in the absence of transport processes, which can later be employed in simulations of the CO bulk oxidation reaction.

2. Experimental Section

Figure 1 presents a schematic illustration of the dual thin-layer flow cell.³⁷ It consists of two compartments connected by four capillaries. In the upper compartment, the electrochemical reaction takes place at the horizontally oriented polycrystalline (pc) Pt working electrode, forming the upper wall of the compartment. The diameter of the electrode area accessible to the electrolyte is 6 mm, equivalent to a surface area of 0.283 cm². The bottom side of the compartment with the electrolyte inlet and the four outlets for the electrolyte flow is separated from the electrode side by a flexible O-ring of approximately 0.05 mm in thickness, which also serves as spacer and determines the height of the flow cell. In the lower compartment, the electrolyte flows over a porous Teflon membrane, which separates the electrochemical cell from a mass spectrometer system and which is permeable for volatile species only.¹⁰

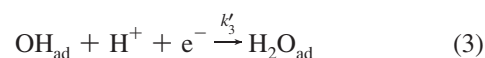
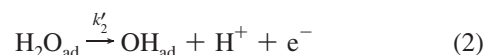
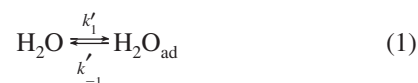
The supporting electrolyte, 0.5 M sulfuric acid, was prepared from Millipore Milli-Q water (resistivity >18 MΩ cm) and ultrapure sulfuric acid (Merck suprapur) and deaerated by high-purity Ar gas (Westfalen Gase, N 6.0) or saturated with CO (Messer-Griesheim N 4.7) through it. CO saturated electrolyte was passed through the flow cell at a flow rate of 5 μL s⁻¹, which was controlled by a syringe pump connected to the outlet

of the flow cell. The potential was controlled by a Princeton Applied Research model 263A potentiostat. A saturated calomel electrode (SCE) served as reference electrode. All potentials, however, are quoted versus that of the reversible hydrogen electrode (RHE). The working electrode was electrochemically cleaned by several potential cycles between 0.03 and 1.36 V at a sweep rate of 100 mV s⁻¹, until a stable base voltammogram was obtained.

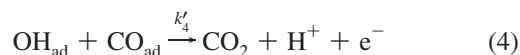
In the CO_{ad} stripping experiments, the electrochemically cleaned electrode surface was exposed to CO saturated (~1 mM CO) base solution at 0.06 V for about 5 min, directly after potential cycling and stopping the potential scan at 0.06 V. Afterward, the flow-cell was rinsed with CO-free base electrolyte for 15 min before the potential was scanned from 0.06 to 1.16 V at a sweep rate of 10 mV s⁻¹. In the CO bulk oxidation experiments, CO saturated electrolyte flows continuously through the cell, and potential cycling was started after 5 min preadsorption time. Further details about the CO_{ad} stripping experiments and the continuous CO bulk oxidation measured in this type of flow cell can be found in refs 7, 38 and 39.

3. Modeling Approach and Numerical Simulation

Electrocatalytic Reaction Mechanism. Previous studies on the mechanism of the CO electro-oxidation over pc-Pt electrodes generally assume a Langmuir–Hinshelwood mechanism, where oxygen-containing species formed on the Pt surface react with adsorbed CO to form CO₂. For the oxygen-containing species, adsorbed OH, formed from the dissociation of adsorbed H₂O, is generally assumed as acting agent under these conditions.^{40,41} The dissociation of H₂O is reversible and described by the following three reactions:



The index “ad” denotes adsorbed species. Irreversible CO₂ formation then occurs by



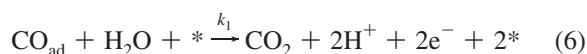
On the basis of these DFT calculations, Janik et al. concluded that on Pt(111) both the availability of OH_{ad} (water activation) and the reaction between CO_{ad} and OH_{ad} control the rate, with the latter being dominant at higher overpotentials, where a critical coverage of OH_{ad} species is reached.⁴¹ Assuming instantaneous adsorption of H₂O on a vacant site³⁰ and finite, potential-dependent rate constants for the other reactions, each of the rate constants can be modeled via the Butler–Volmer (BV) relation using

$$k'_i = A'_i \exp\left(\frac{zF\alpha_i}{RT} E\right) \quad i = 2, 3, 4 \quad (5)$$

where k_i is the respective rate constant, R is the gas constant, F is the Faraday constant, T is the temperature, and z is the number of electrons transferred, here $z = 1$.⁹ E presents the potential, and α_i is the transfer coefficient.

Saravanan et al. used irreversible CO adsorption, ignoring any CO desorption in their Monte Carlo simulations.³⁰ However, these assumptions are not suitable to simulate ideal preadsorption in a flow cell (initial coverage of CO and H₂O are unity and zero, respectively), because in reality the initial CO_{ad} coverage is slightly less than unity,¹⁰ which is also a prerequisite to activate the oxidizing reaction. More precisely, the initial CO_{ad} coverage is slightly less than the saturation coverage obtained in the presence of CO in the electrolyte,^{42–44} but throughout this article relative coverages will be used, where by definition $\theta = 1$ at saturation, rather than absolute coverages, which are related to the number of surface atoms.

The four elementary reactions described above (eqs 1–4) can be subsumed in the following overall reaction, which includes also the active surface sites and which contains only a single effective BV-type rate constant k_1 :



Here, “*” denotes an empty active surface site. The resulting two vacant surface sites, after desorption of CO₂, are neighbored to each other. During a voltammetry experiment, the potential $E(t)$ is linearly varied in time, t . In this simulation, the sweep time is chosen as an independent variable, and therefore k_1 is modeled by introducing the sweep time into eq 5:

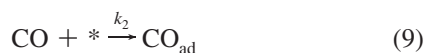
$$k_1 = A_1 \exp\left(\frac{zF\alpha_1\nu}{RT}t\right) \quad (7)$$

Here, $z = 2$, and the sweep rate, ν , is 10 mV s⁻¹. The corresponding reaction rate can then be expressed as follows:

$$r = k_1 c_{\text{CO}_{\text{ad}}} c_*^\beta = k_1 \rho_A \theta_{\text{CO}} [\rho_A (1 - \theta_{\text{CO}})]^\beta \quad (8)$$

$c_{\text{CO}_{\text{ad}}}$ and c_* are the concentrations of CO_{ad} and vacant sites on the electrode, respectively, and β is the reaction order with respect to the vacant sites (> 0). ρ_A is the density of catalytic sites, and θ_{CO} is the (relative) coverage of CO_{ad} on the electrode surface. The effect of the solvent H₂O on the reaction rate is neglected due to its excess presence.

Taking into account the CO adsorption and desorption process as follows, the full reaction mechanism includes three irreversible reactions:



Here, k_2 and k_3 are the rate constants. There are only five kinetic parameters, which can be determined from the experimental data in this mechanism as described by eqs 6, 9, and 10. According to the model, water adsorption depends on the presence of vacant sites, and a completely CO covered surface inhibits electro-

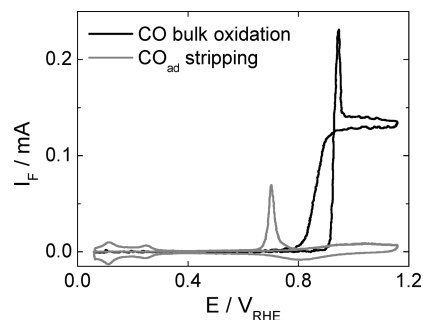


Figure 2. Measured Faradaic current signals during CO_{ad} monolayer oxidation (gray) and continuous CO bulk oxidation (black) for a single positive-going potential sweep (sweep rate 10 mV s⁻¹).

catalytic oxidation. The supply of vacancies is determined by the competition of CO adsorption and CO oxidation, which causes the pronounced hysteresis of the Faradaic current in CO bulk oxidation (Figure 2). At higher temperatures, CO desorption needs to be included as well.^{42,45,46}

For simulation of CO_{ad} stripping, CO adsorption (eq 9) can be neglected, because there is basically no CO in the electrolyte. With increasing potential, a small but incrementally increasing fraction of vacant Pt sites is provided by both CO desorption and slow CO oxidation. Once CO oxidation is triggered after reaching a crucial potential, the CO coverage begins to decrease rapidly.

Although CO desorption is very slow,^{30,42} it plays a significant role in initiating CO oxidation for both CO_{ad} stripping and CO bulk oxidation, and thus affects the position of the Faradaic current onset. Another factor influencing the peak current is the reaction order of vacant sites, as will be discussed below.

Modeling Species Diffusion. In modeling diffusion in liquids, diffusion coefficients are primarily based on hydrodynamic and activated-state models.⁴⁷ A number of empirical correlations, which provide the best available prediction, permit one to estimate diffusivities in terms of more easily measured properties such as viscosity and molar volume. The Wilke–Chang equation,^{48,49} for instance, provides diffusivities for diluted solutions, that is, small concentrations of a nondissociating solute A in B, and can therefore be applied for estimating the diffusivities (m² s⁻¹) of CO and CO₂ in the electrolyte:

$$D_{\text{AB}} = 7.4 \times 10^{-15} (\phi_B M_B)^{1/2} \frac{T}{\mu_B V_{\text{bA}}^{0.6}} \quad (11)$$

V_{bA} is the molar volume of the solute A in cm³ mol⁻¹ as liquid at its boiling point under standard conditions, μ_B is the viscosity, M_B is the molar mass of the solvent (water), and ϕ_B is the “association parameter” of the solvent. The latter accounts for hydrogen bonding in the solvent, and its value depends on nature of the solvent (e.g., for water, it is 2.26⁵⁰).

The diffusivity of the proton (H⁺) is estimated by an empirical equation, using the species’ molecular conductivity:

$$D_A = \frac{\lambda_+ RT}{z_+^2 F^2} \quad (12)$$

Here, λ_+ is the molecular conductivity of the ion A in the liquid at a given concentration; z_+ is the charge number of the ion A.

Geometric Models of the Cell. For a three-dimensional system, the diffusion displacement l can be described by

$$l^2 = 6 \cdot D_{AB} \cdot t \quad (13)$$

based on the Einstein relation. Here, D_{AB} is the diffusion coefficient of the corresponding species, and t is the diffusion time. On the basis of the diffusion models used, the diffusivities of CO, CO₂, and H⁺ in the aqueous solution are estimated to be in the ranges of $D_{CO} \approx (0.8-1) \times 10^{-9} \text{ m}^2 \text{ s}^{-1}$, $D_{CO_2} \approx (1-2) \times 10^{-8} \text{ m}^2 \text{ s}^{-1}$, and $D_{H^+} \approx (0.8-1) \times 10^{-5} \text{ m}^2 \text{ s}^{-1}$ under the present conditions. For the thin-layer flow cell used in this study, the diffusion times in the z -direction (Figure 1c) are then estimated by eq 13 to be $t_{CO} \approx (4.2-5.3) \times 10^{-1} \text{ s}$, $t_{CO_2} \approx (1.4-4.2) \times 10^{-2} \text{ s}$, and $t_{H^+} \approx (4.2-5.2) \times 10^{-5} \text{ s}$. For the present experimental situation, the mean residence time of the electrolyte in the reaction chamber is

$$\tau = \frac{\text{volume of the reaction chamber}}{\text{volumetric flow rate at the inlet}} = 0.38 \text{ s} \quad (14)$$

Because in the radial direction of the cell (x -direction), CO diffusion is much slower than the electrolyte flow, we only need to consider diffusion normal to the electrode surface. Furthermore, because of the high diffusivity and the much higher concentration of H⁺, we can neglect concentration gradients in H⁺ along the z -direction.

In this work, several transport models of increasing complexity are employed to describe the electrolyte transport (Figure 1d), starting with a zero-dimensional (0D) model (no transport) as the most simple case. The one-dimensional (1D) model is used to reveal the effect of mass transport in x -direction, which is the primary flow direction. The two-dimensional (2D) model, with z as second spatial coordinate, which is the direction normal to the electrode, is applied to examine the effect of CO diffusion toward the electrode. A three-dimensional (3D) model is finally employed to study the impact of the inhomogeneous convection in radial direction away from the inlet caused by the four separate outlets and the impact of CO diffusion in the x - y plane due to this inhomogeneous flow on Faradaic current, and, aside from that, to predict the three-dimensional CO spatial distribution in the cell.

For describing the CO_{ad} stripping behavior, only the 0D model was applied, because there is no continuous supply of CO ("batch reactor"). The reaction kinetic parameters are fitted to optimize the agreement between the simulated and experimentally measured profiles of the Faradaic current.

Convective Transport Models. In the 1D model, a mean flow velocity, v_{mean} , is used based on the mean residence time of the electrolyte:

$$v_{\text{mean}} = \frac{\text{inner radius of the reaction chamber}}{\tau} = 9.2 \times 10^{-3} \text{ m s}^{-1} \quad (15)$$

In the 2D model, a parabolic velocity profile of a fully developed laminar flow is assumed as

$$v_x = \frac{6 \cdot v_m}{h^2} (z^2 - h^2/4) \quad (16)$$

where h is the height of the reaction cell ($5 \times 10^{-5} \text{ m}$), and the origin of the coordinate x , which goes along the main flow direction, is located at the middle of the inlet port (Figure 1a).

In the 3D model, the full Navier–Stokes equations are solved:

$$\begin{aligned} & \rho \left(\frac{\partial v_x}{\partial t} \right) - \eta \left(\frac{\partial^2 v_x}{\partial x^2} + \frac{\partial^2 v_x}{\partial y^2} + \frac{\partial^2 v_x}{\partial z^2} \right) + \\ & \rho \left(v_x \frac{\partial v_x}{\partial x} + v_y \frac{\partial v_x}{\partial y} + v_z \frac{\partial v_x}{\partial z} \right) + \frac{\partial p}{\partial x} = \rho g_x \\ & \rho \left(\frac{\partial v_y}{\partial t} \right) - \eta \left(\frac{\partial^2 v_y}{\partial x^2} + \frac{\partial^2 v_y}{\partial y^2} + \frac{\partial^2 v_y}{\partial z^2} \right) + \\ & \rho \left(v_x \frac{\partial v_y}{\partial x} + v_y \frac{\partial v_y}{\partial y} + v_z \frac{\partial v_y}{\partial z} \right) + \frac{\partial p}{\partial y} = \rho g_y \\ & \rho \left(\frac{\partial v_z}{\partial t} \right) - \eta \left(\frac{\partial^2 v_z}{\partial x^2} + \frac{\partial^2 v_z}{\partial y^2} + \frac{\partial^2 v_z}{\partial z^2} \right) + \\ & \rho \left(v_x \frac{\partial v_z}{\partial x} + v_y \frac{\partial v_z}{\partial y} + v_z \frac{\partial v_z}{\partial z} \right) + \frac{\partial p}{\partial z} = \rho g_z \\ & \frac{\partial v_x}{\partial x} + \frac{\partial v_y}{\partial y} + \frac{\partial v_z}{\partial z} = 0 \end{aligned} \quad (17)$$

where \mathbf{v} is the velocity vector, ρ is the density of the fluid, and p is the pressure. $G = \{g_x, g_y, g_z\}$ is a body force term, here representing gravity. η denotes the dynamic viscosity of the 0.5 M sulfuric acid solution. Because of the low mass fraction of CO in the electrolyte ($\sim 2.8 \times 10^{-5}$), there is no substantial influence of the dissolved gas on the fluid properties. Hence, the calculation of the flow field was based on the fluid properties of the pure 0.5 M sulfuric acid solution.

Because of the small Reynolds number (maximum Reynolds number for the present cell is ~ 13), the laminar flow model can be employed to calculate the velocity distribution. The average inlet flow rate of $6.37 \times 10^{-3} \text{ m}^3 \text{ s}^{-1}$ was based on the volumetric flow rate of the experiment.

Species Transport Models. To predict the evolution of CO coverage, the following mass balance equation was imposed on the catalytic surface, based on the reaction mechanism described by eqs 6, 9, and 10:

$$\frac{d\theta_{CO}}{dt} = -k_1 \theta_{CO} [(1 - \theta_{CO}) \rho_A]^\beta + k_2 c_{CO} (1 - \theta_{CO}) - k_3 \theta_{CO} \quad (18)$$

Here, c_{CO} is the concentration of CO in the fluid near the electrode.

On the basis of the steady-state CO_{ad} coverage and a vanishing oxidation rate at the preoxidation potential regime, the initial coverage of CO_{ad} on the pc-Pt electrode can be derived from eq 18:

$$-k_3 \theta_{CO}^0 + k_2 c_{CO} (1 - \theta_{CO}^0) = 0 \Rightarrow \theta_{CO}^0 = \frac{k_2 c_{CO}}{k_2 c_{CO} + k_3} \quad (19)$$

To predict the concentration distribution of bulk species for both CO_{ad} stripping and CO bulk oxidation, the following governing equations of mass transport, which determine the motion in the system, are used:

$$\begin{aligned} \frac{\partial(c_i)}{\partial t} &= r_i \quad \text{on the electrode surface} \\ \frac{\partial(c_i)}{\partial t} + \text{div}(\mathbf{v}c_i) &= \text{div}(D_i \nabla(c_i)) \quad \text{in the reaction cell} \end{aligned} \quad (20)$$

Here, c_i is the concentration of species i , that is, CO, CO₂, H⁺, given in mol m⁻³ in the fluid and in mol m⁻² on the surface. r_i is the chemical production rate, that is, $r_{\text{CO}} = -r$, $r_{\text{CO}_2} = r$, and r is given by eq 8. Furthermore, \mathbf{v} is the velocity vector, $\nabla(c_i)$ is the concentration gradient, and D_i is the diffusion coefficient of species i , respectively.

Relation between Faradaic Current and Surface Reaction.

In the general case, where the CO_{ad} coverage may vary spatially, the total charge Q passed through the pc-Pt electrode surface is given by

$$Q = F \int_A n \, dA \quad (21)$$

where n is the location-dependent number of electrons exchanged at the electrode surface during the reaction (from time 0 to t , in mol m⁻²), F is the Faraday constant, and A is the geometric area of the electrode surface. Based on the definition of the surface reaction rate and the assumed reaction mechanism, eq 6, the production rate of electrons is

$$\frac{dn}{dt} = 2r \quad (22)$$

Hence, the relation between the Faradaic current and the reaction rate can be written as

$$I_F = \frac{dQ}{dt} = \frac{d(F \int n \, dA)}{dt} = F \int \frac{dn}{dt} \, dA = F \int 2r \, dA \quad (23)$$

Substituting eq 8, we have

$$I_F = F \int_A 2k_1 \theta_{\text{CO}} \rho_A [(1 - \theta_{\text{CO}}) \rho_A]^\beta \, dA \quad (24)$$

The commercial code FLUENT is used to simulate the continuous flow field of the electrolyte in the 3D model. A finite element method is applied to calculate the mass transport and chemical reactions in the 0D, 1D, 2D, and 3D models by using COMSOL MULTIPHYSICS.

4. Results and Discussion

The measured Faradaic current exhibits three characteristic features as a function of voltage and time, as shown in Figure 2. First, CO oxidation is set at different voltages for CO_{ad} stripping and CO bulk oxidation, with a shift of 200 mV to higher voltage in the latter experiment. Second, for CO_{ad} stripping, the peak current is only 0.07 mA at a peak potential of 0.7 V. The current disappears once the preadsorbed CO_{ad} is completely consumed. For CO bulk oxidation, the peak current is much higher, about 0.23 mA at a potential of 0.92 V. The difference between the two maximum oxidation currents is explained by the continuous supply of CO to the electrode surface in the latter case. Third, for CO bulk oxidation, the

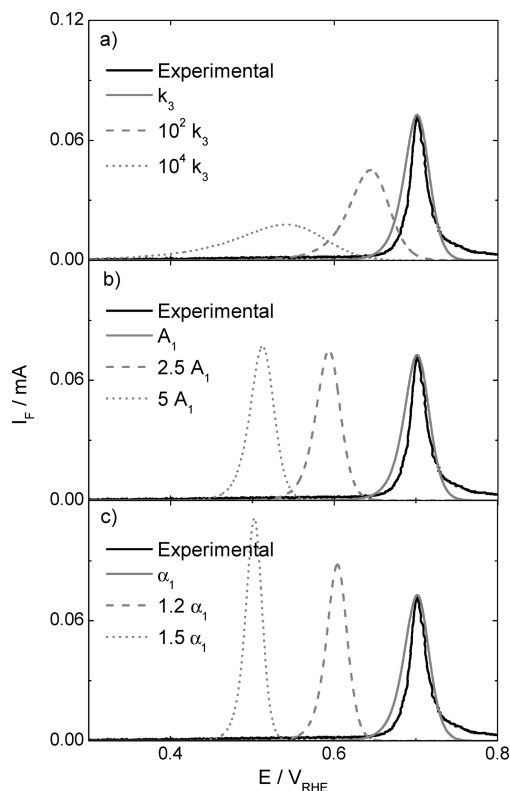


Figure 3. Simulations illustrating the effect of varying (a) the rate constant for CO desorption k_3 , (b) the preexponential factor A_1 , and (c) the transfer coefficient α_1 on the Faradaic current during CO_{ad} monolayer oxidation (0D model).

Faradaic current rapidly declines after peaking and reaches a quasi steady-state with an almost constant current around 0.14 mA, which decreases only slightly at potentials exceeding 1.02 V. In the negative-going potential scan, the CO oxidation current is about stable up to 0.91 V. Next, it rapidly decreases and vanishes at 0.7 V. The curves largely resemble previous data obtained on pc-Pt electrodes.^{8,21,22,51–53}

0D Model of CO_{ad} Stripping. Because there is no spatial variation of the surface coverage and hence of the local current density in CO_{ad} stripping, the kinetic parameter of reaction 6 can then be derived from the results of the CO_{ad} stripping experiments using the 0D model, which considers only the reaction kinetics. These results represent the basis of the simulations of the CO bulk oxidation reaction.

The effects of the remaining parameters, k_3 and k_1 (i.e., A_1 and α_1 in eq 7), on the peak current are shown in Figure 3. An increase in desorption rate, that is, increasing k_3 , broadens the peak and shifts it to smaller potentials. According to eq 10, a larger k_3 increases the number of surface vacancies, which affects the oxidation rate (eq 8). As a result, the current peak occurs at lower potentials, but the lower CO coverage and smaller k_1 in the peak region decreases its height and broadens it. From previous experimental data, it is known, however, that the desorption rate and rate constant at room temperature are rather low and can be neglected except for very high coverages.^{42,45,46}

Increasing A_1 and α_1 (eq 7) narrows the peak and shifts it to lower potentials, due to the increased oxidation rate.

Because the local current density does not depend on the spatial coordinates in CO_{ad} stripping, eq 24 leads to

$$I_F = F \int_A 2k_1 \theta_{CO} \rho_A [(1 - \theta_{CO}) \rho_A]^\beta dA = 2FA_{cat} k_1 \theta_{CO} [(1 - \theta_{CO}) \rho_A]^\beta \quad (25)$$

Here, $A_{cat} = \rho_A \cdot A$ defines the total amount of pc-Pt surface sites, given in moles, on the accessible electrode surface area. Because the current in the CO_{ad} stripping experiment can be related to the CO_{ad} coverage, the coverage of CO_{ad} as a function of time can be calculated on the basis of the experimental data, assuming that all CO is completely consumed at $t = 80$ s.

$$\theta_{CO} \Big|_t = 1 - \frac{\int_{t=0}^t I_F dt}{\int_{t=0}^{t=80 \text{ s}} I_F dt} \quad (26)$$

Introducing eq 26 into eq 19 then yields

$$I_F \Big|_t = 2FA_{cat} A_1 \exp\left(\frac{2F\alpha_1 v}{RT} t\right) \left(1 - \frac{\int_{t=0}^t I_F dt}{\int_{t=0}^{t=80 \text{ s}} I_F dt}\right) \times \left(\rho_A \frac{\int_{t=0}^t I_F dt}{\int_{t=0}^{t=80 \text{ s}} I_F dt}\right)^\beta \quad (27)$$

This leads to the following general relation between the parameters A_1 and α_1 :

$$\frac{2F\alpha_1 v}{RT} t + \ln(A_1) = \ln\left(\frac{I_F \Big|_t}{2FA_{cat} \left(1 - \frac{\int_{t=0}^t I_F dt}{\int_{t=0}^{t=80 \text{ s}} I_F dt}\right) \left(\rho_A \frac{\int_{t=0}^t I_F dt}{\int_{t=0}^{t=80 \text{ s}} I_F dt}\right)^\beta}\right) \quad (28)$$

On the basis of that equation, optimum kinetic parameters can be extracted from the experimental data. Table 1 shows the fitted kinetic parameters for $\beta = 1$ and $\beta = 2$.⁵⁴

TABLE 1: Kinetic Parameters for CO_{ad} Stripping and Bulk Oxidation for Different Models

model parameters	0D model	1D model	2D model	3D model
$A_1/m^2 \text{ mol}^{-1} \text{ s}^{-1}$	110	3210	150	150
α_1	0.098	0.233	0.093	0.093
$k_2/m^2 \text{ mol}^{-1} \text{ s}^{-1}$		1.26×10^{-4}	4.0×10^{-4}	2.0
k_3/s^{-1}	2.0×10^{-7}	2.6×10^{-3}	1.0×10^{-7}	1.0×10^{-7}
β	1	2	1	1

TABLE 2: Mass Transport Governing Equations and Boundary Conditions of Different Models

governing equations	boundary conditions		
	reaction wall	inlet	outlet
0D model	$\frac{\partial c_i}{\partial t} = r_i$		
1D model	$\frac{\partial c_i}{\partial t} + v_m \frac{\partial c_i}{\partial x} = D \frac{\partial^2 c_i}{\partial x^2} + r_i$	$c_i = c_{i0}$	$-(\partial c_i)/(\partial x) = 0$
2D model	$\frac{\partial c_i}{\partial t} + v_x \frac{\partial c_i}{\partial x} = D \frac{\partial^2 c_i}{\partial x^2} + D \frac{\partial^2 c_i}{\partial z^2}$	$D(\partial c_i)/(\partial z) = r_i$	$c_i = c_{i0}$ and $-(\partial c_i)/(\partial x) = 0$
3D model	$\frac{\partial c_i}{\partial t} + v_x \frac{\partial c_i}{\partial x} + v_y \frac{\partial c_i}{\partial y} + v_z \frac{\partial c_i}{\partial z} = D \left(\frac{\partial^2 c_i}{\partial x^2} + \frac{\partial^2 c_i}{\partial y^2} + \frac{\partial^2 c_i}{\partial z^2} \right)$	$D(\partial c_i)/(\partial z) - c_i v_z = r_i$	$c_i = c_{i0}$ and $-(\partial c_i)/(\partial z) = 0$

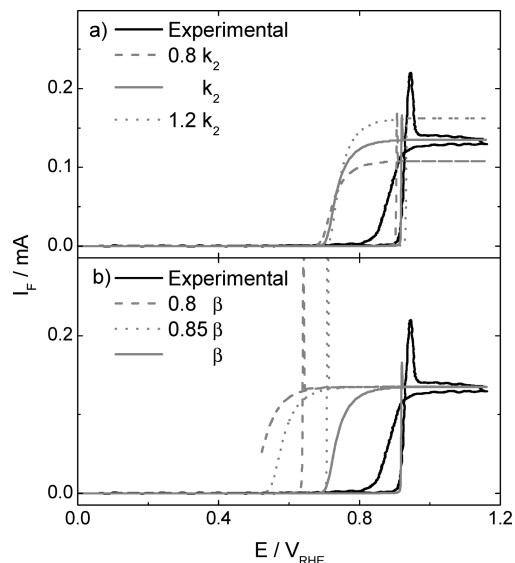


Figure 4. Simulations illustrating the effect of varying (a) the rate constant for CO adsorption k_2 and (b) the rate exponent for vacant Pt sites β on the Faradaic current during continuous CO oxidation (0D model).

0D Model Study of CO Bulk Oxidation. The purpose of including the 0D model for the description of the CO bulk oxidation is to estimate the minimum CO adsorption rate constant k_2 in the absence of mass transport limitations (Table 2).

In CO bulk oxidation experiments (Figure 4), the Faradaic current is negligible at potentials below 0.9 V in the positive-going scan, then increases rapidly at > 0.9 V, passes through a distinct peak with a maximum at 0.95 V, and then decreases again to a constant value at higher potentials, which is commonly known as “mass transport limited” current.^{10,22,53–55} The distinct peak results from the combined oxidation of preadsorbed CO and CO adsorbing from the bulk.^{10,54,55} The quasi steady-state Faradaic current at potentials higher than that of the peak, I_F^s , is limited by the adsorption rate k_1 . Under these conditions, the CO coverage approaches zero, and consequently CO desorption can be ignored. In the 0D model, where we assume that I_F^s is controlled by the reaction kinetics without any consideration of mass transfer limitation, the minimum adsorption rate constant k_2 can be determined via the following equations:

$$\begin{cases} \theta_{\text{CO}} \cong 0 \\ I_{\text{F}}^{\text{ss}} = F \int_A 2k_1\theta_{\text{CO}}\rho_{\text{A}}[(1 - \theta_{\text{CO}})\rho_{\text{A}}]^{\beta} dA \Rightarrow I_{\text{F}}^{\text{ss}} \cong 2FA_{\text{cat}}k_2c_{\text{CO}} \\ -k_1\theta_{\text{CO}}[(1 - \theta_{\text{CO}})\rho_{\text{A}}]^{\beta} + k_2c_{\text{CO}}(1 - \theta_{\text{CO}}) - k_3\theta_{\text{CO}} \cong 0 \end{cases} \quad (29)$$

The rate constant k_2 derived this way is used as an initial guess for the more complex models.

Moreover, the reaction order of vacant Pt sites β can be used to fit the pronounced hysteresis of the peak current of the CO bulk oxidation reaction. The effects of varying the rate of CO adsorption, k_2 , and the reaction order, β , in eq 8 are shown in Figure 4. The adsorption rate constant k_2 clearly affects the peak current and the quasi steady-state current (Figure 4a). An increase of the CO adsorption rate k_2 results in a disappearance of the peak, but an increase of the quasi steady-state current. On the other hand, the reaction order of active Pt surface sites, β , has considerable influence on the hysteresis in the Faradaic current, which increases for larger values of β .

All kinetic parameters were optimized to equally predict the experimental data of CO_{ad} stripping and CO bulk oxidation by the 0D model. The resulting values are listed in Table 1.

1D Model Study of CO Bulk Oxidation. On the basis of the estimation of the residence and diffusion times, effects of the mass transfer on the Faradaic current for CO bulk oxidation are likely. The kinetic data of the 0D model were extracted from the experimental data with the tacit assumption that the Faradaic current is purely controlled by the reaction kinetics. The resulting kinetic parameters were introduced in the 1D model. In these simulations, a variation of the mean velocity was found to have a relatively small effect on the $I_{\text{F}}(t)$ profile, as shown in Figure 5a. This is reasonable, because these parameters were derived setting mass transport to zero. On the other hand, it is clear that not all features of the experimental results can be reproduced by the 1D model using the kinetic data of the 0D model. For instance, a current is still predicted at a potential as low as 0.72 V in the negative-going scan ($t = 160$ s), whereas experimentally no current was measured at potentials lower than 0.8 V in that scan direction. Therefore, it is expected that the kinetic parameters need to be adjusted, where the set derived by the 0D model will serve as an initial guess.

To reveal the effect of convection along the major flow direction, the spatial coordinate x , on the Faradaic current, the 1D model is used. In this case, the mean velocity will be an important factor, as revealed by Figure 5b, which shows I_{F} curves for varying mean velocities for a newly adjusted set of kinetic parameters as given in Table 1.

In these simulations, no adequate set of kinetic parameters was found to produce acceptable agreement between computed and experimentally measured I_{F} profiles using the mean velocity estimated from the experimentally determined residence time (eq 14). The experimental I_{F} profile could only be reproduced by decreasing the inlet velocity drastically. In other words, the 1D model failed in giving an adequate description of the coupled reaction and transport process. The rather small mean velocity derived from these fits $v_{\text{mean,fit}} = 1.86 \times 10^{-3} \text{ m s}^{-1}$, indicates that another transport process with a slower time scale dominates the potentiodynamic bulk oxidation process.

2D Model Study of CO Bulk Oxidation. Simulations with the 2D model were carried out to study the effect of diffusion along the direction normal to the electrode. The second spatial coordinate is along the main flow direction. All kinetic data were adjusted again to optimize the agreement between experimental and simulated I_{F} profiles, using the experimentally

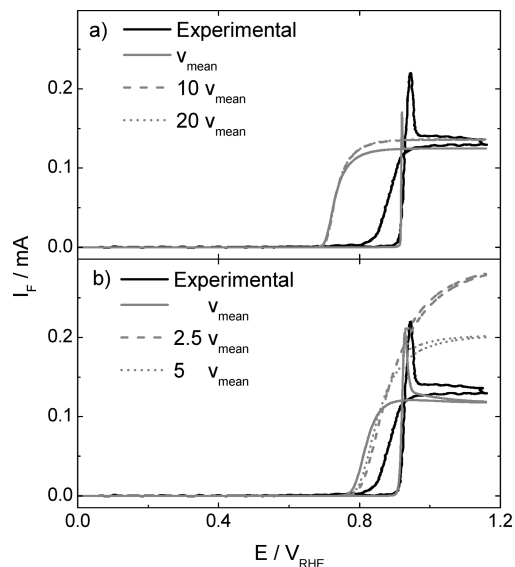


Figure 5. Set of simulations illustrating the effect of varying the inlet velocity on the Faradaic current during continuous CO oxidation in two different reaction and transport regimes, using the 1D model and the kinetic parameters derived in the 0D model: (a) in a regime dominated by the reaction kinetics (high mean velocities) and (b) in a regime dominated by mass transfer (low mean velocities). The kinetic data are listed in Table 1.

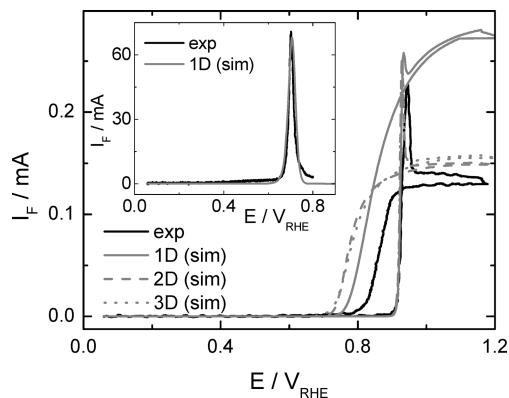


Figure 6. Set of simulations illustrating the effect of using different transport models on the resulting Faradaic current profiles during CO_{ad} stripping (inset) and CO bulk oxidation for different transport models, using optimized kinetic parameters in each case (see Table 1). For comparison, the experimental data are included as well (black).

derived inlet velocity (eq 16). The resulting values are given in Table 1. The first major result of these simulations is that all major features of the experimental I_{F} profiles, both for CO_{ad} stripping and for CO bulk oxidation, can be reproduced within the uncertainties of the experimental conditions. These uncertainties result in particular from the not very well-defined height of the cell (z -direction), which is determined by the flexible spacer and which directly affects the important contribution of diffusion to mass transfer in that direction.

In Figure 6, we illustrate the influence of different transport models on the numerically predicted I_{F} profiles. It clearly shows that taking into account the influence of the velocity field the simulation result of the 1D model differs from that of the 0D model. Likewise, involving mass transfer by diffusion in the z -direction leads to results in the 2D model simulations different from those in the 1D model.

Figure 7a reveals the temporally and spatially (along the main flow direction and along the height above the electrode) resolved profiles of the CO_{ad} coverage on the electrode for CO bulk

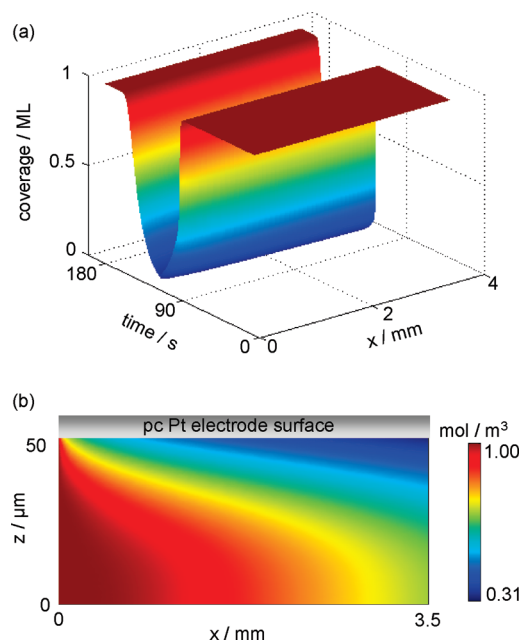


Figure 7. (a) Plot of the local CO_{ad} coverage during CO bulk oxidation as a function of the sweep time along the main flow direction using optimized kinetic parameters. (b) Plot of the predicted 2D CO concentration profile in the electrolyte during CO bulk oxidation under quasi steady-state conditions (sweep time 115 s) along the main flow direction, x , and at varying heights above the electrode, z . The 2D model simulations were performed using optimized kinetic parameters (Table 1).

oxidation. In Figure 7b, the 2D CO_{ad} concentration profile under steady-state conditions (constant Faradaic current at $E > 0.97$ V) is shown. Interestingly, the CO_{ad} coverage is not constant in the potential regime of almost constant Faradaic currents, but decreases with increasing potential ($t < 116$ s) and vice versa ($t > 116$ s). Under steady-state conditions, the CO profile in the fluid varies along the z -direction, as expected for a mass transport process that is dominated by diffusion (Figure 7b). Furthermore, the spatial variation of the CO concentration in the electrolyte along the x -axis, in particular just above the electrode surface, illustrates the strong effect of CO diffusion on the CO bulk oxidation. This implies that the overall electrocatalytic CO bulk oxidation is partly mass-transfer limited.

Figure 8 shows the temporal and spatial (z -direction) evolution of the CO_2 concentration at the position of the outlet. It is closely correlated to the current–time profile of the Faradaic current, I_{F} . Interestingly, the variation along the z -direction is not very pronounced. This has important consequences on the CO_2 detection, because due to the intermixing of the electrolyte upon passing through the connecting capillaries the mass spectrometric detection averages over the total CO_2 content in the electrolyte. If there is little variation in the CO_2 concentration along the vertical axis, as in the present case, this averaging of the evolving CO_2 concentration has little effect, and, therefore, the evolving CO_2 corresponds closely to the one measured by the mass spectrometer.

3D Model Study of CO Bulk Oxidation. Finally, a time-resolved three-dimensional simulation was applied to also include mass transport in the x – y plane and to identify other possible three-dimensional transport effects, which could have been neglected so far due to the simplifying assumptions made in the 1D and 2D models. For these simulations, we used the same kinetic parameters as derived in the 2D model simulations.

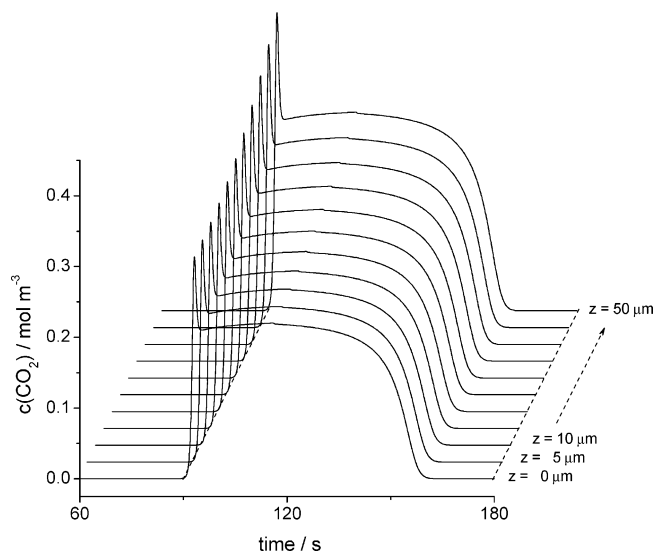


Figure 8. Plot of the predicted CO_2 concentration at the outlet position as a function of sweep time and vertical height above the electrode, z . The 2D model simulations were performed using optimized kinetic parameters (Table 1).

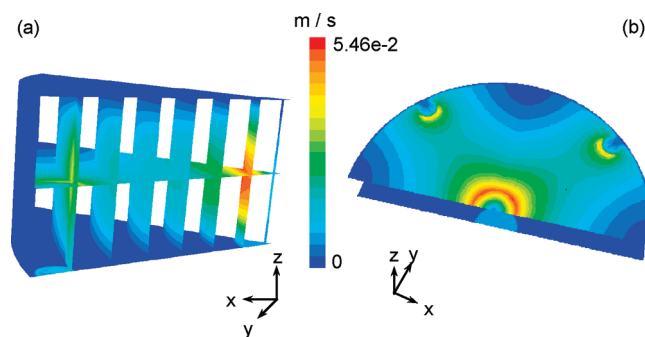


Figure 9. 3D display of the predicted 3D electrolyte velocity distribution. (a) Slices of the velocity fields along z at different constant distances x from the inlet in a 45° segment of the flow cell (see dotted line in (b)); and (b) lateral velocity distribution in the x – y plane at $z = 25 \mu\text{m}$. The 3D model simulations were performed using the kinetic parameters optimized in the 2D simulations (Table 1).

Figure 9 illustrates the predicted velocity distribution of the electrolyte flow in the entire cell in a 45° segment of the cell. Slices of the velocity distribution along the z -direction at different constant distances from the inlet position (Figure 9a) reveal a drastic variation of the flow velocity. Close to both the inlet and the outlets, the maximum velocity ($5.46 \times 10^{-2} \text{ m s}^{-1}$) is about 10 times higher than the average inlet velocity. Figure 9b shows the velocity distribution in an x – y plane at a constant vertical distance $z = 2.5 \mu\text{m}$ above the bottom of the cell, where both the inlet and the outlet capillaries enter the cell, and $47.5 \mu\text{m}$ away from the electrode (along the z -axis). As illustrated in this figure, rather low flow velocities exist in the zones between two adjacent outlets. This may lead to enhancement of local mass transfer limitations, due to low convection of the electrolyte in those zones.

The temporal evolution of the three-dimensional concentration profiles can be predicted by using the time-resolved 3D model. The resulting CO concentrations are illustrated in Figure 10 for two different sweep times (potentials). Figure 10a shows the CO concentration profiles at the time $t = 93.2$ s, which is right at the current peak. At this time, concentration gradients in the z -direction are just established, due to the depletion of the dissolved CO close to the electrode surface caused by the onset

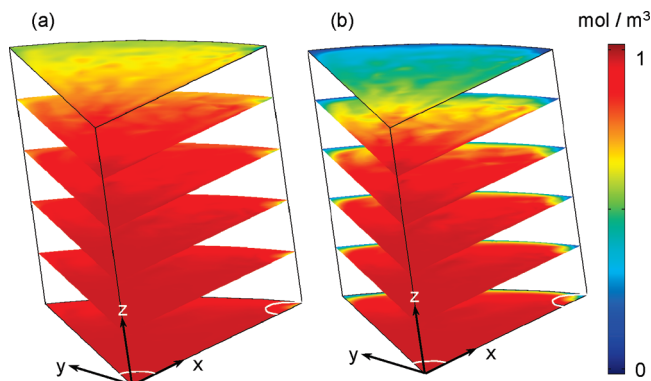


Figure 10. Spatially resolved CO concentration in the electrolyte (mol m^{-3}) at x - y planes at different heights during CO bulk oxidation. (a) At the onset of the CO oxidation reaction ($t = 93.2$ s); and (b) under quasi steady-state conditions at high potentials ($t = 115$ s). The 3D model simulations were performed using the kinetic parameters optimized in the 2D simulations (Table 1).

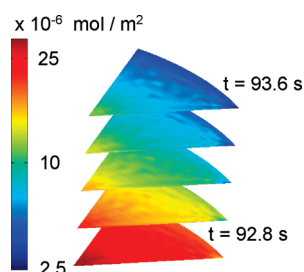


Figure 11. Spatially resolved evolution of the CO_{ad} coverage (mol m^{-2}) with time at the onset of the CO bulk oxidation reaction ($t = 92.8$ – 93.6 s). The 3D model simulations were performed using the kinetic parameters optimized in the 2D simulations (Table 1).

of the electrocatalytic oxidation. The predicted evolution of the CO_{ad} coverage during that time, $t = 92.8$ – 93.6 s, is presented in Figure 11. This figure reveals significant variations in the local CO_{ad} coverage, as expected from the variation in CO concentrations in the electrolyte close to the electrode surface. (Note that saturation coverage corresponds to $\sim 17 \times 10^{-6} \text{ mol m}^{-2}$.) At higher sweep times, just above the onset of the CO oxidation reaction, the amount of CO adsorbed on the electrode surface is increasingly depleted from the outside to the inside, because the CO concentration in the electrolyte close to the surface decreases along the flow direction after the onset of the CO oxidation reaction.

CO concentration profiles similar to those in Figure 10a are presented in Figure 10b, showing the concentration distribution of CO when the Faradaic current has reached a pseudo steady-state situation ($t = 115$ s). Under these conditions, the CO concentration exhibits not only strong gradients along the z -direction, but there are also pronounced concentration gradients in the x - y plane, in particular close to the electrode and close to the outlets. The 3D gradients of the CO concentration illustrate the pronounced influence of mass transfer on the Faradaic current. Furthermore, on the other hand, the simulation results also demonstrate that variation of the cell dimensions, in particular of the cell height, h , significantly affects the concentration profiles and therefore the Faradaic current. Accordingly, slight variations in the geometry of the experimental setup, in particular in the cell height, h , can lead to considerable changes in the measured Faradaic current.

Although these plots provide clear evidence for the existence of more or less pronounced three-dimensional variations in the CO concentration patterns during CO bulk oxidation, the 3D

and the 2D model leads to almost identical predictions for the Faradaic current profiles, as illustrated in Figures 7b and 10b, respectively. This leads to the conclusion that CO diffusion in the x - y plane has only little effect on the CO bulk oxidation characteristics, and hence the Faradaic current in this flow cell. Hence, both the 3D and the 2D, but not the 1D model, provide a sufficiently precise description of the complex spatio-temporal structure in the CO concentration and in the CO_{ad} coverage to accurately predict the Faradaic current as a function of potential (sweep time). Because the computational costs of the time-resolved 3D simulation are extensive, the 2D model is the model of choice for many purposes. This is particularly true for the determination of adequate kinetic parameters, which can be determined with sufficient precision from the 2D simulations. In contrast, detailed understanding of the possible contributions from pronounced spatial inhomogeneities in the reaction process requires 3D simulations. Hence, the approach chosen in the present study, from simple to complex models, is not only justified from a very basic point of view, to better understand the role and contribution of different transport processes, but is appropriate also from an economic point of view.

5. Conclusions

A three-step electrocatalytic reaction mechanism including the influence of surface coverage on adsorption, desorption, and oxidation of CO was coupled with transport models of increasing complexity to numerically simulate the reaction behavior on a polycrystalline Pt electrode in a dual thin-layer flow cell. The potentiodynamic oxidation of a preadsorbed CO monolayer (“ CO_{ad} stripping”) and the oxidation of CO in a continuous flow of a CO saturated electrolyte (“CO bulk oxidation”), where the Faradaic current was monitored during potential sweeps, were analyzed for this specific cell geometry. In the model, the kinetic parameters have been adapted step-by-step from the 0D to the 3D transport model. The results from 0D CO_{ad} stripping simulation were used as an initial guess for the more sophisticated models including two- and three-dimensional flow analysis. The CO adsorption rate, k_2 , determines the quasi steady-state Faradaic current, in the kinetically limited regime.

The 1D model is not able to cover the mass transport characteristics of the cell, because the oxidation rate and, hence, the Faradaic current are much more influenced by diffusion of CO toward the electrode than by convection along the flow direction. The 2D and 3D models quantitatively predict all features of the Faradaic current as a function of potential. Because of the inhomogeneities of the flow cell used in this study, the spatial and temporal gradients in the fluid and on the electrode need to be taken into account for a thorough interpretation of the experimental data. CO concentrations and coverage depend on the position in the cell and on the electrode, respectively. While the Faradaic current is primarily controlled by the reaction kinetics in the CO_{ad} stripping experiment and during the startup of the reaction in the CO bulk oxidation experiment, the reaction rate is rapidly affected by transport processes in the fluid at high reaction rates.

The time-resolved, 3D model also revealed strong concentration and velocity gradients as well as gradients in surface coverage in the spatial planes, which are located in parallel to the electrode plane and on the electrode, respectively. These gradients are mainly determined by the positions of the inlet and outlets. Even though, for the present application, the two-dimensional model is able to predict all experimental features and is much less CPU time-consuming. It should be noted that this reduction of the transport model (from 3D to 2D) needs to

be evaluated again for operation of the cell at very different conditions or for different cell geometries. Because the Faradaic current measured is a result of various pronounced and nonlinear interactions between different physical and chemical processes, compensating effects may lead to the wrong conclusion that 2D models are always sufficient for the simulation of electrocatalytic reactions in such kind of electrocatalytic cells.

The models and computer codes developed can now not only be used to interpret the experimental findings, but also to explore the consequences of specific further operating conditions. Future development will focus on deriving the reaction kinetics from the molecular behavior on the electrocatalytic active electrode, for example, by coupling with density functional theory (DFT) calculations rather than determining them by fitting to experimentally measured data. Current work is devoted to both of these directions.

Acknowledgment. We are grateful to Dr. Z. Jusys for stimulating discussions. Financial support of this work came from the Baden-Württemberg Stiftung within the “Kompetenznetz Funktionelle Nanostrukturen” (Project B9).

Nomenclature

α_1	transfer coefficient
β	reaction order with respect to the vacant sites
λ_+	molecular conductivity of the ion A, $\text{m}^2 \text{s}^{-1} \text{mol}^{-1}$
ϕ_B	association parameter
μ_B	viscosity of the solution, Pa s
τ	mean residence time of the electrolyte in the reaction chamber, s
η	density of the fluid, kg m^{-3}
ρ_A	density of total catalytic sites, mol m^{-2}
η	dynamic viscosity, Pa s
θ_{CO}	coverage of CO_{ad} on the electrode surface
θ_{CO}^0	initial coverage of CO_{ad} on the electrode surface
A	area of the reaction surface, m^2
A_1	pre-exponential factor
A_{cat}	total amount of accessible Pt sites, mol
c_i	bulk concentration of species i , mol m^{-3}
c_{CO}	concentration of CO near the electrode surface, mol m^{-3}
$c_{\text{CO}_{\text{ad}}}$	concentration of adsorbed CO, mol m^{-2}
D_{AB}	diffusivity for small concentrations of A in B, $\text{m}^2 \text{s}^{-1}$
D_{CO}	diffusivity for small concentrations of CO, $\text{m}^2 \text{s}^{-1}$
D_{CO_2}	diffusivity for small concentrations of CO_2 , $\text{m}^2 \text{s}^{-1}$
D_{H^+}	diffusivity for small concentrations of H^+ , $\text{m}^2 \text{s}^{-1}$
D_i	diffusion coefficient of species i , $\text{m}^2 \text{s}^{-1}$
$\nabla(c_i)$	concentration gradient of species i
E	voltage, V
F	Faraday constant, C mol^{-1}
\mathbf{G}	body force, N
h	height of the electrochemical cell, m
I_{F}	Faradaic current, A
I_{F}^{ss}	quasi steady-state Faradaic current of CO bulk oxidation, A
l	diffusion displacement, m
k_1/k_{-1}	rate constants for H_2O adsorption/desorption, s^{-1}
k_2'	rate constant for dissociation of H_2O , s^{-1}
k_3'	rate constant for formation of H_2O , s^{-1}
k_4'	rate constant of irreversible formation of CO_2 , s^{-1}
k_1	rate constant for CO oxidation, s^{-1}
k_2	rate constant for CO adsorption, s^{-1}
k_3	Rate constant for CO desorption s^{-1}

n	location-dependent number of electrons passed through the electrode surface during the reaction, per surface area, mol m^{-2}
M_B	molar mass of solvent, kg mol^{-1}
p	pressure, Pa
Q	charge of the Faradaic current through electrode, C
*	active surface site
c_*	concentration of active Pt sites, mol m^{-2}
R	gas constant, $\text{J K}^{-1} \text{mol}^{-1}$
R_i	production rate by chemical reactions
r	oxidation reaction rate, $\text{mol m}^{-2} \text{s}^{-1}$
T	temperature, K
t	time, s
t_{CO}	diffusion time in the z -direction for CO, s
t_{CO_2}	diffusion time in the z -direction for CO_2 , s
t_{H^+}	Diffusion time in the z -direction for H^+ , s
\mathbf{v}	velocity vector, m s^{-1}
v	sweep rate, V s^{-1}
v_{inlet}	inlet velocity, m s^{-1}
v_{mean}	average flow velocity, m s^{-1}
v_x	flow velocity along the x -direction, m s^{-1}
V_{bA}	molar volume of the solute A, $\text{cm}^3 \text{mol}^{-1}$
z	number of electrons transferred
z_+	charge number of the ion

References and Notes

- (1) Bard, A. J.; Faulkner, L. R. *Electrochemical Methods - Fundamentals and Applications*; John Wiley & Sons: New York, 1980.
- (2) Hamann, C. H.; Hamnett, A.; Vielstich, W. *Electrochemistry*, 2nd ed.; Wiley VCH: Weinheim, 2007.
- (3) Thomas, J. M.; Thomas, W. J. *Principles and Practice of Heterogeneous Catalysis*; VCH: Weinheim, 1997.
- (4) Chen, S.; Kucernak, A. *J. Phys. Chem. B* **2004**, *108*, 3262–3276.
- (5) Schneider, A.; Colmenares, L.; Seidel, Y. E.; Jusys, Z.; Wickman, B.; Kasemo, B.; Behm, R. J. *Phys. Chem. Chem. Phys.* **2008**, *10*, 1931–1943.
- (6) Seidel, Y. E.; Schneider, A.; Jusys, Z.; Wickman, B.; Kasemo, B.; Behm, R. J. *Faraday Discuss.* **2008**, *140*, 167–184.
- (7) Lindström, R.; Seidel, Y. E.; Jusys, Z.; Gustavsson, M.; Kasemo, B.; Behm, R. J. *J. Electroanal. Chem.* **2010**, *644*, 90–102.
- (8) Breiter, M.; Hoffmann, K. Z. *Elektrochem.* **1960**, *64*, 462–467.
- (9) Bard, A. J.; Faulkner, L. R. *Electrochemical Methods*; Wiley & Sons: New York, 1980.
- (10) Jusys, Z.; Kaiser, J.; Behm, R. J. *Phys. Chem. Chem. Phys.* **2001**, *3*, 4650–4660.
- (11) Beden, B.; Lamy, C.; De Tacconi, N. R.; Arvia, A. J. *Electrochim. Acta* **1990**, *35*, 691–704.
- (12) Vielstich, W. *Encyclopedia of Electrochemistry - Interfacial Kinetics and Mass Transport*; VCH: Weinheim, 2003.
- (13) Iwasita, T. *Handbook of Fuel Cells, Vol. 2: Electrocatalysis*; John Wiley & Sons: Chichester, 2003; Chapter 41, pp 603–624.
- (14) Batista, E. A.; Iwasita, T.; Vielstich, W. *J. Phys. Chem. B* **2004**, *108*, 14216–14222.
- (15) Arenz, M.; Mayrhofer, K. J.; Stamenkovic, V.; Blizanac, B. B.; Tomoyuki, T.; Ross, P. N.; Markovic, N. M. *J. Am. Chem. Soc.* **2005**, *127*, 6819–6829.
- (16) Lu, G. Q.; Lagutchev, A.; Dlott, D. D.; Wieckowski, A. *Surf. Sci.* **2005**, *585*, 3–16.
- (17) Mayrhofer, K. J.; Arenz, M.; Blizanac, B. B.; Stamenkovic, V.; Ross, P. N.; Markovic, N. M. *Electrochim. Acta* **2005**, *50*, 5144–5154.
- (18) Morschl, R.; Bolten, J.; Bonnefont, A.; Krischer, K. *J. Phys. Chem. C* **2008**, *112*, 9548–9551.
- (19) Fromondi, I.; Scherson, D. *Faraday Discuss.* **2008**, *140*, 59–68.
- (20) Heinen, M.; Chen, Y.-X.; Jusys, Z.; Behm, R. J. *Electrochim. Acta* **2007**, *53*, 1279–1289.
- (21) Heinen, M.; Chen, Y. X.; Jusys, Z.; Behm, R. J. *Electrochim. Acta* **2007**, *52*, 5634–5643.
- (22) Stonehart, P. *J. Electroanal. Chem.* **1967**, *15*, 239–244.
- (23) Bergelin, M.; Herrero, E.; Feliu, J. M.; Wasberg, M. *J. Electroanal. Chem.* **1999**, *467*, 74–84.
- (24) Koper, M. T. M.; Schmidt, T. J.; Markovic, N. M.; Ross, P. N. *J. Phys. Chem. B* **2001**, *105*, 8381–8386.
- (25) Holzbecher, E.; Halseid, R.; Jusys, Z.; Fuhrmann, J.; Behm, R. J. Modellierung von Dünnschichtzellen - Thin Layer Flow Cell Modelling. Conference Proceeding, 2006.

- (26) Fuhrmann, J.; Zhao, H.; Holzbecher, E.; Langmach, H.; Chojak, M.; Halseid, R.; Jusys, Z.; Behm, R. *J. Phys. Chem. Chem. Phys.* **2008**, *10*, 3784–3795.
- (27) Fuhrmann, J.; Linke, A.; Langmach, H.; Baltruschat, H. *Electrochim. Acta* **2009**, *55*, 430–438.
- (28) Fuhrmann, J.; Zhao, H.; Holzbecher, E.; Langmach, H. *J. Fuel Cell Sci. Technol.* **2008**, *5*, 021008/1-021008/10.
- (29) Koper, M. T. M.; Jansen, A. P. J.; van Santen, R. A. *J. Chem. Phys.* **1998**, *109*, 6051.
- (30) Saravanan, C.; Markovic, N. M.; Head-Gordon, M.; Ross, P. N. *J. Chem. Phys.* **2001**, *114*, 6404–6412.
- (31) Saravanan, C.; Koper, M. T. M.; Markovic, N. M.; Head-Gordon, M.; Ross, P. N. *Phys. Chem. Chem. Phys.* **2002**, *4*, 2660–2666.
- (32) Housmans, T. H. M.; Hermse, C. G. M.; Koper, M. T. M. *J. Electroanal. Chem.* **2007**, *607*, 69–82.
- (33) Bonnefont, A.; Varela, H.; Krischer, K. *ChemPhysChem* **2003**, *4*, 1260–1263.
- (34) Kee, R. J.; Coltrin, M. E.; Glarborg, P. *Chemically Reacting Flow*; Wiley-Interscience: New York, 2003.
- (35) Deutschmann, O. *Handbook of Heterogeneous Catalysis*, 2nd ed.; Ertl, G., Knözinger, H., Schüth, F., Weitkamp, J., Eds.; Wiley-VCH: New York, 2007; Chapter 6.6.
- (36) Pineda, M.; Imbihl, R.; Schimansky-Geier, L. *Physica A* **2010**, *389*, 1178–1188.
- (37) Jusys, Z.; Massong, H.; Baltruschat, H. *J. Electrochem. Soc.* **1999**, *146*, 1093–1098.
- (38) Seidel, Y. E.; Müller, M.; Jusys, Z.; Wickman, B.; Hanarp, P.; Kasemo, B.; Hörmann, U.; Kaiser, U.; Behm, R. *J. Electrochem. Soc.* **2008**, *155*, K171–K179.
- (39) Seidel, Y. E.; Jusys, Z.; Wickman, B.; Kasemo, B.; Behm, R. *J. ECS Trans.* **2010**, *25*, 91–102.
- (40) Markovic, N. M. *Electrocatalysis*; Wiley & Sons: Chichester, 2003; pp 386–393.
- (41) Janik, M. J.; Neurock, M. *Electrochim. Acta* **2007**, *52*, 5517–5528.
- (42) Heinen, M.; Chen, Y.-X.; Jusys, Z.; Behm, R. *J. ChemPhysChem* **2006**, *8*, 2484–2489.
- (43) Cuesta, A.; del Carmen Perez, M.; Rincón, A.; Gutierrez, C. *ChemPhysChem* **2006**, *7*, 2346–2351.
- (44) Cuesta, A.; Couto, A.; Rincón, A.; Perez, M. C.; Lopez-Cudero, A.; Gutierrez, C. *J. Electroanal. Chem.* **2006**, *586*, 184–195.
- (45) Davies, J. C.; Nielsen, R. M.; Thomsen, L. B.; Chorkendorff, I.; Logadottir, A.; Lodziana, Z.; Nørskov, J. K.; Li, W. X.; Hammer, B.; Longwitz, S. R.; Schnadt, J.; Vestergaard, E. K.; Vang, R. T.; Besenbacher, F. *Fuel Cells* **2003**, *4*, 1–11.
- (46) Davies, J. C.; Tsoitridis, G. *J. Phys. Chem. C* **2008**, *112*, 3392–3397.
- (47) Bird, R. B.; Stewart, W. E.; Lightfoot, E. N. *Transport Phenomena*, 2nd ed.; Wiley & Sons: New York, 2007; Chapter 3, pp 75–104.
- (48) Wilke, C. R.; Chang, P. *AIChE J.* **1955**, *1*, 264–270.
- (49) Fisk, P. R.; Jonathan, P.; Whitstable, K. *Comprehensive Chemical Kinetics*; Elsevier: Amsterdam, 1999; pp 543–571.
- (50) Green, D. W.; Perry, R. H. *Perry's Chemical Engineers Handbook*, 8th ed.; The MacGraw Hill Co.: New York, 2008.
- (51) Gilman, S. *J. Phys. Chem.* **1963**, *67*, 1989–1905.
- (52) Markovic, N. M.; Grgur, B. N.; Lucas, C. A.; Ross, P. N. *J. Phys. Chem. B* **1999**, *103*, 487–495.
- (53) Stalnionis, G.; Tamasauskaite-Tamasiunaite, L.; Pautieniene, V.; Jusys, Z. *J. Electroanal. Chem.* **2006**, *590*, 198–206.
- (54) Schmidt, T. J.; Gasteiger, H. A.; Behm, R. *J. Electrochem. Soc.* **1999**, *146*, 1296–1304.
- (55) Gasteiger, H. A.; Markovic, N. M.; Ross, P. N. *J. Phys. Chem.* **1995**, *99*, 8290–8301.

JP106967S